Coupled electron and nuclear motion in strong laser fields

Lucas E. Aebersold,[1] Inga S. Ulusoy,[2,1,*] and Angela K. Wilson[1,†]

[1]*Department of Chemistry, Michigan State University, 578 South Shaw Lane, East Lansing, Michigan 48824-1322, USA*

[2]*Theoretical Chemistry, Institute of Physical Chemistry, Heidelberg University, Im Neuenheimer Feld 229, 69120 Heidelberg, Germany*

(Received 5 December 2018; revised manuscript received 1 July 2019; published 9 August 2019)

Electron motion in molecules can be initiated by a laser pulse and, through the induced charge migration, can, in turn, trigger a response from the nuclei. The generated electron-nuclear wave packets can quickly decohere, but also lead to recurrence of coherences. Presented here is a quantum dynamics study of H_2 and LiH in strong fields. No separation of electronic and nuclear motion is assumed, and no precomputed potential energy surface is required. It is shown that electron and nuclear motion are strongly coupled through the laser-pulse excitation, and already moderate nuclear excitation can substantially impact the electron dynamics. Through the full quantum dynamical treatment, coherence properties of electronic and nuclear wave function can be investigated. The nuclear motion leads to decoherences while it can also introduce recurrence of coherences.

DOI: 10.1103/PhysRevA.100.023406

I. INTRODUCTION

Experimental efforts to initiate and monitor electronic motion in molecules have achieved tremendous progress in the past two decades: from the first generation of attosecond pulse trains in 2001 [1,2], through the first imaging of single-electron wave functions [3] and generation of laser pulses with pulse durations of only 6 as [4], to the observation and control of electron migration in iodoacetylene [5], and, very recently, the acceleration of chemical reactions [6]. Attosecond science has begun to receive more attention from the chemistry and molecular physics community. One pertinent goal of chemists, the control of chemical reactions, seems viable through charge-directed chemistry. This field is inspired by early experiments of Weinkauf *et al.* [7–9]; initially, an electronic wave packet is created either through ionization or electronic excitation. This electronic wave packet leads to nonstationary electron dynamics through charge migration [10–12], resulting in an electron-nuclear potential that changes on a femtosecond to attosecond time scale. Through this modulating potential, nuclear motion can be initiated and, ideally, be driven to trigger a desired process such as a specific fragmentation of a molecule or even chemical reactions. Conversely, the motion of the nuclei can facilitate and enhance electronic processes, such as charge-resonance enhanced ionization (CREI) [13–16], the generation of even harmonics for centrosymmetric molecules [17], or in chemical reactions [6].

Attosecond spectroscopy is very closely connected with strong-field physics, as attosecond laser pulses are commonly generated through the electronic response to strong incident laser fields (typically around 10^{14} W/cm^2), such as in high-order harmonic generation (HHG). Recent combined experimental and theoretical approaches [18,19] demonstrate that the electron-nuclear dynamics in H_2 and H_2^+ exhibit very strong electron-nuclear coupling in electric fields. The phase of the overlapping eigenstates that compose the initiated wave packet leads to very complex dynamics; these can only be understood in a fully quantum-mechanical description of both electronic and nuclear degrees of freedom.

It is shown here that the molecular response to strong laser fields entails both nuclear and electronic excitations (even on a time scale of a few tenths of femtoseconds), which can be coupled to each other, forming molecular rather than electronic or vibrational excitations. In the spirit of vibronic or excitonic states, these initiated wave packets generate signatures in the potential, resembling quantum beating. Furthermore, absorption spectra are obtained in which both electronic and nuclear transition energies are encoded, and they provide excellent agreement with experimental data.

The multiconfiguration electron-nuclear dynamics (MCEND) method [20–22] is employed, where the electron-nuclear wave function is described as a sum of products of determinants for the electrons and Hartree products for the nuclei. Both the determinants and the Hartree products are time dependent, as are the state coefficients that signify the population of each product. Similar as in the multiconfiguration time-dependent Hartree (MCTDH) method [23] for nuclear dynamics, and the multiconfiguration time-dependent Hartree-Fock (MCTDHF) method [24–26] for electron dynamics, the equations of motion (EOM) for wave functions and coefficients are obtained through the time-dependent variational principle (TDVP). This leads to a very efficient, though nonlinear, description of the time evolution of the electron-nuclear system, and allows the simulation of systems that cannot be treated by solving the time-dependent Schrödinger equation directly. Such exact calculations have been carried out by Bandrauk and co-workers [13,27,28] and in the framework of exact factorization (XF) techniques [29–31]. Another approach that treats electron and nuclear dynamics on the same footing is the electron-nuclear dynamics (END) [32] approach, where

*inga.ulusoy@pci.uni-heidelberg.de
†akwilson@msu.edu

 ©2019 American Physical Society

extensions to including electron correlation and nuclear quantum effects have been proposed [33,34]. Furthermore, there are density-based methods available that allow a simultaneous evolution of electronic and nuclear degrees of freedom (DOF) [35–37], but these also treat the nuclei classically. Other extensions of MCTDH(F), similar in spirit to MCEND, have been proposed [38,39], which utilize a different partitioning of electronic and nuclear subspaces to facilitate the evaluation of the EOMs. A formulation within a mean-field configuration-interaction (CI) scheme is also available [40].

II. MULTICONFIGURATION ELECTRON-NUCLEAR DYNAMICS

In the MCEND method, the molecular wave function is represented as a sum over products of determinants $\Phi_{J_e}(\mathbf{r},t)$ for the electrons and Hartree products $\Phi_{J_n}(\mathbf{R},t)$ for the nuclei:

$$\Psi(\mathbf{r},\mathbf{R},t)=\sum_{J_e}^{\mathrm{ord}}\sum_{J_n}A_{J_eJ_n}(t)\Phi_{J_e}(\mathbf{r},t)\Phi_{J_n}(\mathbf{R},t), \tag{1}$$

$$\Phi_{J_e}(\mathbf{r},t)=\left|\varphi_{j_1^e}(\mathbf{r}_1,t)\varphi_{j_2^e}(\mathbf{r}_2,t)\cdots\varphi_{j_{N_e}^e}\left(\mathbf{r}_{N_e},t\right)\right|, \tag{2}$$

$$\Phi_{J_n}(\mathbf{R},t)=\prod_{k}^{N_k}\varphi_{j_k^n}(R_k,t), \tag{3}$$

with composite index $J_e=(j_1^e,j_2^e,\ldots,j_{N_e}^e)$ and $J_n=(j_1^n,j_2^n,\ldots,j_{N_k}^n)$. The spin orbitals (SOs) $\varphi_{j_i^e}$ and single-particle functions (SPFs) $\varphi_{j_k^n}$ constitute the single-particle basis and are time dependent, adapting to the optimal representation at each time step. The MCEND molecular Hamiltonian is expressed as

$$\hat{H}(\mathbf{r},\mathbf{R})=\hat{T}_e(\mathbf{r})+\hat{T}_n(\mathbf{R})+V_{ee}(\mathbf{r})+V_{en}(\mathbf{r},\mathbf{R})+V_{nn}(\mathbf{R}). \tag{4}$$

Here, $\hat{H}_e(\mathbf{r})=\hat{T}_e(\mathbf{r})+V_{ee}(\mathbf{r})$ is defined as the electronic Hamiltonian (where $V_{en}(\mathbf{r},\mathbf{R})$ is not contained in $\hat{H}_e(\mathbf{r})$, contrary to the usual definition), and $\hat{H}_n(\mathbf{R})=\hat{T}_n(\mathbf{R})+V_{nn}(\mathbf{R})$ is the nuclear Hamiltonian. The coupling between electronic and nuclear DOF is contained in $V_{en}(\mathbf{r},\mathbf{R})$. The time dependence of the SOs, SPFs, and coefficients $A_{J_eJ_n}(t)$ that relate the single-particle to the many-particle basis are obtained from the TDVP:

$$i\dot{A}_{J_eJ_n}=\sum_{L_e}^{\mathrm{ord}}\sum_{L_n}\left\langle\Phi_{J_e}\Phi_{J_n}\middle|\hat{H}\middle|\Phi_{L_e}\Phi_{L_n}\right\rangle A_{L_eL_n} \tag{5}$$

$$=\sum_{L_e}^{\mathrm{ord}}\left\langle\Phi_{J_e}\middle|\hat{H}_e\middle|\Phi_{L_e}\right\rangle A_{L_eL_n}+\sum_{L_n}\left\langle\Phi_{J_n}\middle|\hat{H}_n\middle|\Phi_{L_n}\right\rangle A_{L_eL_n}$$

$$+\sum_{L_e}^{\mathrm{ord}}\sum_{L_n}\left\langle\Phi_{J_e}\Phi_{J_n}\middle|V_{en}\middle|\Phi_{L_e}\Phi_{L_n}\right\rangle A_{L_eL_n}, \tag{6}$$

$$i\dot{\varphi}_{j_i^e}=(1-P^e)(\rho^e)^{-1}\langle\hat{H}_e+V_{en}\rangle\varphi_{j_i^e}, \tag{7}$$

$$i\dot{\varphi}_{j_k^n}=(1-P^n)(\rho^n)^{-1}[\hat{H}_n+\langle V_{en}\rangle]\varphi_{j_k^n}. \tag{8}$$

The projection operators P^e and P^n project onto the space spanned by the SOs and SPFs so that $P^e=\sum_{i=1}^{N_e}|\varphi_{j_i^e}\rangle\langle\varphi_{j_i^e}|$ and $P^n=\sum_{k=1}^{N_k}|\varphi_{j_k^n}\rangle\langle\varphi_{j_k^n}|$. The reduced electronic and nuclear density matrices are given by ρ^e and ρ^n, and $\langle\hat{H}_e+V_{en}\rangle$ and $\langle V_{en}\rangle$ are the mean fields [21]. No nuclear rotational terms are included in the Hamiltonian, which is supported by the alignment of the molecular axis in strong fields as in the applications targeted here. The MCEND wave function is very flexible, and can be systematically improved by adding molecular orbitals (MOs) and SPFs. The naming convention follows the one in electronic structure theory: (number of electrons, number of MOs, number of SPFs).

Using a wave function obtained from a propagation in imaginary time as the initial state, the absorption spectrum of a molecule can be generated with MCEND by employing a time-dependent Hamiltonian. The electric field coupling is described in the semiclassical dipole approximation in the length gauge. By computing the autocorrelation function, $\langle\Psi(\mathbf{r},\mathbf{R},t=0)|\Psi(\mathbf{r},\mathbf{R},t)\rangle$, and taking its inverse Fourier transform after the laser pulse has been switched off, the frequency components of the time-dependent electron-nuclear wave function can be resolved. Here, the molecule is excited using a short, nonresonant laser pulse, so that a superposition state is generated that contains components of the accessible eigenstates of the molecule. The frequency components of the autocorrelation function (and their weights) then provide insights into the energies of the eigenstates and transition moments from the ground state. Such absorption spectra are computed for H_2 and LiH, where the laser pulse takes the following form:

$$\mathbf{E}(t)=\mathbf{E}_0\sin^2\left(\frac{\pi t}{2\sigma}\right)\cos(\omega_0 t), \tag{9}$$

with $\mathbf{E}_0$ the initial pulse height for a specific orientation along the x, y, or z direction, 2σ the pulse width, and ω_0 the carrier frequency. For very short pulses, the vector potential would need to be included as to avoid nonzero-area pulses.

The approach here does not describe electronic and vibrational continuum states (the primitive basis that is used at this point does not allow a treatment of continuum states). For one, the electronic basis is chosen as a Gaussian basis distributed on a grid; and Gaussian basis functions lead to a trapping of charge rather than allowing charge to occupy the highly delocalized continuum states. Furthermore, the grid basis that represents the primitive nuclear basis in principle can describe dissociation, but would need to be extended much further in range than what is included in the calculation (and, ideally, be capped with a complex absorbing potential). However, the laser-pulse parameters were chosen such that the intensity lies at or below $10^{14}\,\mathrm{W/cm^2}$, as this is generally considered a threshold beyond which ionization and dissociation channels are fully accessible for a molecular system. Below this threshold, tunnel ionization and, similarly, dissociation also take place, but at a much lower percentage. For example, the possibility to generate high-order harmonic spectra necessarily implies that negative charge can be moved far away from the molecule through tunnel ionization. For the electron-nuclear spectra presented here, the parameters were chosen to minimize these effects; this becomes apparent from considering the nuclear difference density as shown below, which is well contained on the nuclear grid, thus

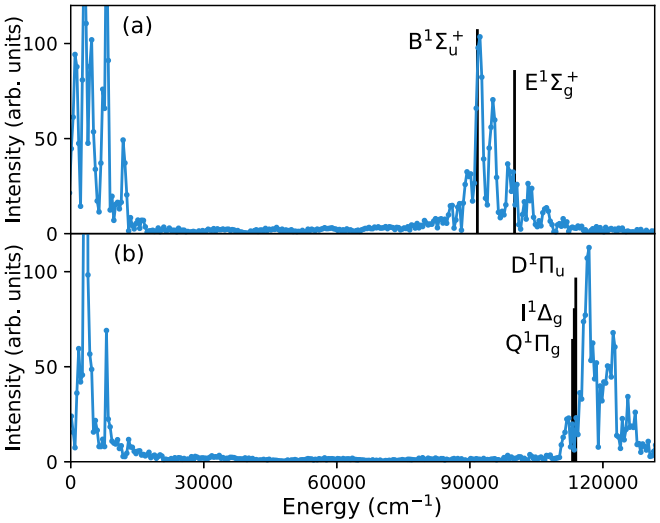

FIG. 1. Absorption spectra for H_2 using the aug-cc-pVDZ basis set at the (221) expansion length, for z (top) and x (bottom) polarization direction. Experimental transition frequencies [41] are marked with black lines.

signifying that, if at all, dissociative channels do not contribute significantly to the dynamics. For the electronic degrees of freedom, such an estimate is much harder to obtain; here, due to the charge trapping, ionization would appear as noise in the spectra. For H_2, it appears that this is not the case, while for LiH, we cannot fully exclude contributions from ionization.

III. RESULTS AND DISCUSSION

A. H_2 excitation spectra

The absorption spectrum of H_2 (laser-pulse parameters $2\sigma = 2.8$ fs, $\omega = 0.416E_h$ (109.5 nm), $I = 10^{14}$ W/cm^2, z direction (along the molecular axis); and $2\sigma = 1.4$ fs, $\omega = 0.555E_h$ (80.9 nm), $I = 10^{14}$ W/cm^2, x direction) is shown in Fig. 1 for a (221) expansion length. The laser-pulse parameters are chosen such that the frequency is off resonant with a specific transition, while being high enough to lie in the vicinity of the electronic excited states. Through the finite pulse length, additional frequency components are included in the laser pulse. The expansion length signifies the use of two time-dependent MOs (four SOs) for two electrons, and one SPF to describe the vibrational DOF.

The computed absorption spectra for H_2 are shown in Fig. 1. There are many features that can be observed in the calculated absorption spectra, where the experimental peak positions are indicated with intensity set to an arbitrary height for better visibility. For one, there is a large cluster of peaks close to the ground-state energy, one centered around 100 000 cm^{-1} (z) and 120 000 cm^{-1} (x). The peaks at higher energies correspond to electronic states that have been populated in the wave packet. The positioning of the peaks is in excellent agreement with the experimental values [41]. However, very noticeable is that there are many smaller peaks located around the excited electronic states at almost equidistant energies from the center peak at $E = 90\,700$ cm^{-1} ($p = z$), $E \approx 110\,000$ cm^{-1} ($p = x$), and also from the ground-state peak

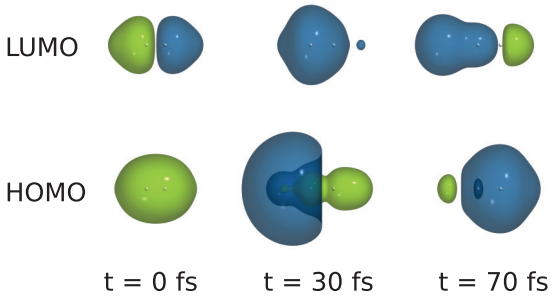

FIG. 2. Graphical representations of the MOs of H_2 before and after laser-pulse excitation in the z polarization direction. The initial MOs resemble the σ and σ^* MOs, which then adapt to the optimal representation at each time step for the time-dependent Hamiltonian.

at $E = 0.0$ cm^{-1}. These peaks result from *nuclear* excited states—vibrational excitations—that have been induced in the diatomic. As H_2 is a homonuclear diatomic with a zero dipole moment, these vibrational excitations cannot be directly induced through the laser pulse. They are a consequence of the electron-nuclear coupling and therefore are induced nonadiabatically through the motion of the electrons, through Raman or other processes. The energy spacing of the peaks is in the range of vibrational transition frequencies, ranging from ≈1000 to ≈4500 cm^{-1}.

The MOs for H_2 during the excitation are shown in Figs. 2 and 3. At time $t = 0$ fs, the MOs clearly resemble the σ and σ^* MOs of H_2. Through the laser-pulse excitation, electron motion is induced in the diatomic and the time-adaptable MOs rotate in Hilbert space, adapting to an optimal representation at the single-particle level of the electron-nuclear wave function. As such, their shapes change as is shown in Figs. 1 and 2, and differ for different polarization directions of the laser pulse.

The electronic excitations that are observed in the spectrum—such as transitions to the $^1\Sigma_u^+$ and $^1\Pi_g$ states—lead to an effective mixing of the MOs, for example, with the σ_{p_z} and $\pi_{p_{x/y}}$ orbitals. It should be noted that these MOs are somewhat analogous to time-independent multiconfiguration self-consistent field MOs in that they do not diagonalize the one-particle reduced density matrix (they are not natural orbitals and as such exhibit fractional occupancies). The multiconfigurational wave function includes determinants in which both electrons are in the lower-lying MO, singly excited

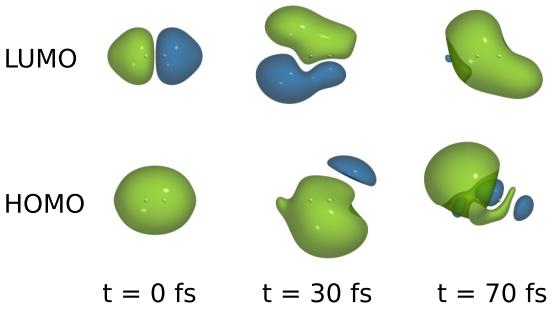

FIG. 3. Graphical representations of the MOs of H_2 before and after laser-pulse excitation in the x polarization direction.

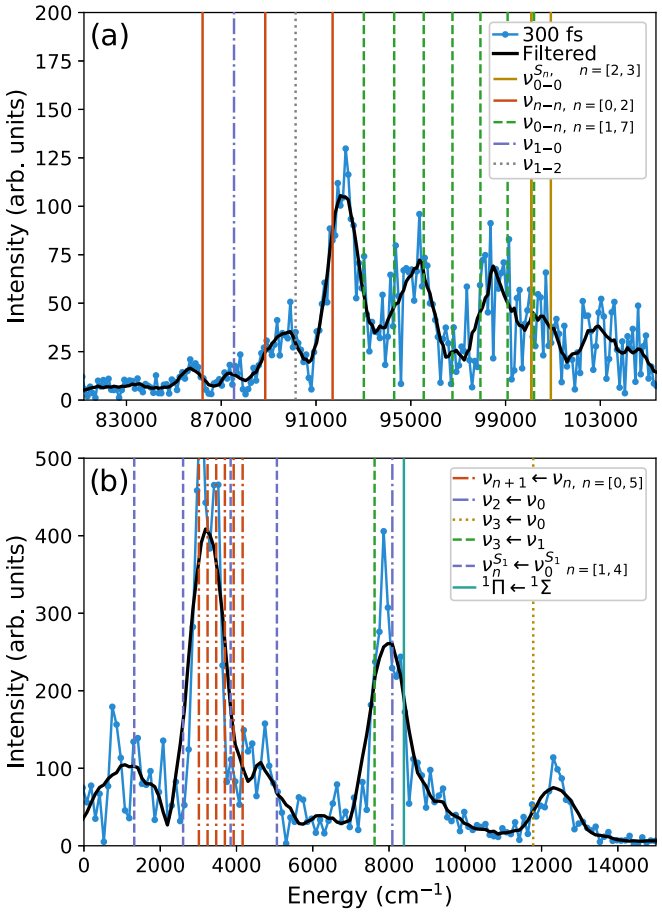

FIG. 4. Electronic and nuclear excitation peaks obtained from H_2 excitation in the z direction run for 300 fs. The Savitzky-Golay filter (black line) is applied to the 300-fs spectrum. Experimental transition energies (cm^{-1}) are overlaid as vertical lines. (a) Energy region around the electronic excited states. (b) Energy region close to the electronic ground state.

determinants, and the doubly-excited determinant in which both electrons are excited into the higher-lying MO. As the MOs are time dependent and adapt to the time-dependent Hamiltonian at each time step, their character changes from pure σ to containing contributions of the higher-lying one-particle states such as the π orbitals.

The detailed absorption spectrum of H_2 is shown in Fig. 4 for a (221) expansion length.

Different possible transitions are marked in the figure together with reference values from the experiment [41,42]. The raw spectrum from a 300-fs propagation is overlaid with a filtered spectrum, using a Savitzky-Golay filter with a window length of 17 points (1770 cm^{-1}) and polynomial order of 3. Both electronic and vibrational transitions are obtained in the spectrum, although the laser-pulse frequency targets electronic excitation (UV) and a direct excitation of vibrations in H_2 is not possible, as it has a zero dipole moment. However, vibrational transitions are induced indirectly through Raman-type processes. In the higher-energy region, the 0-0 transition from the $X^1\Sigma_g^+$ (S_0) ground to the first singlet excited state, $B^1\Sigma_u^+$ (S_1), and from the $E^1\ \Sigma_g^+(S_2)/F^1\Sigma_g^+$ (S_3) $\leftarrow$ $X^1\Sigma_g^+$ transition is indicated by a vertical solid line in red (ν_{0-0}, $B^1\Sigma_u^+ \leftarrow X^1\Sigma_g^+$) and green ($\nu_{0-0}$, $E^1\Sigma_g^+/F^1\Sigma_g^+ \leftarrow X^1\Sigma_g^+$, denoted as $\nu_{0\text{-}0}^{S_n}$). In the following the focus is on vibrational transitions in the ground and $B^1\Sigma_u^+$ states only, as the complexity increases rapidly when more electronic states are considered. The ν_{1-1} and ν_{2-2} $B^1\Sigma_u^+ \leftarrow X^1\Sigma_g^+$ transitions are marked with solid red lines, at energies lower than the $\nu_{0\text{-}0}$ transition as the vibrational energy levels are closer in energy for the excited state (the H_2 bond in this state is weaker). At all of these transition energies, peaks can be found in the simulated spectrum, where the $\nu_{0\text{-}0}$ transition from ground to first excited state results in the highest intensity. Furthermore, in the simulated spectrum there are peaks occurring at energies that correspond to $\nu_{0\text{-}n}$ transitions from electronic ground to first excited state, with $n = [1, 7]$ (dashed line); a peak at the $\nu_{1\text{-}2}$ transition energy (dotted line); and a small peak at the $\nu_{1\text{-}0}$ transition. In the energy region close to the ground state, peaks for vibrational excitations in the electronic ground state can be found (from the vibrational ground state ν_0 to vibrationally excited states, ν_n). Similarly, vibrational transitions in the first electronic excited state also lie in this energy region (from $\nu_0^{S_1}$ to $\nu_n^{S_1}$), and also transitions in higher-lying electronic states. Furthermore, there is a peak at the $C^1\Pi_u \leftarrow B^1\Sigma_u^+$ transition energy which does not originate from the nuclear part of the wave function, as has been confirmed through a Fourier transform of electronic and nuclear position expectation value (this peak is only obtained in the electronic part). The excellent agreement of peak positions with experimental values provides a high level of confidence for these calculations, in that not only qualitative but also quantitative predictions towards the electron-nuclear dynamics can be made.

Through the laser-pulse excitation of the electrons, an electronic wave packet is generated that induces a modulating potential which drives the nuclei from their equilibrium position. As such, a nuclear wave packet is generated that is a superposition of vibrationally excited states (ground state, first vibrational state, and higher-lying states), in the electronic ground state, and also in the electronic excited state(s). The peaks that are observed in the spectrum originate in vibrational transitions in the electronic ground state, and electronic excited states. The magnitude of the peaks is related to the transition dipole moments between the electronic states, and the overlap of the nuclear eigenstate functions in the respective vibrational states, $\langle\phi^n_{\text{initial}}|\phi^n_{\text{final}}\rangle$ (Franck-Condon factors), and the energy difference between the electronic states.

B. LiH excitation spectra

As a second example, a similar calculation was carried out for LiH ($\omega_0 = 0.110E_h$ (414 nm), $I = 1.405\times10^{13}$ W/cm^2, $2\sigma = 2.8$ fs). The resulting spectra are shown in Figs. 5(a) and 5(b). Experimental electronic excitation energies [41,43] are indicated with black lines. The spectra were generated for three different expansion lengths: (421), (431), and (441). The agreement of the (441) transition energies with the experimentally observed transitions is excellent, both for z and x polarization directions, where, depending on the relative polarization of electric field and molecule, different excitations can be observed. The (431) expansion length yields results in

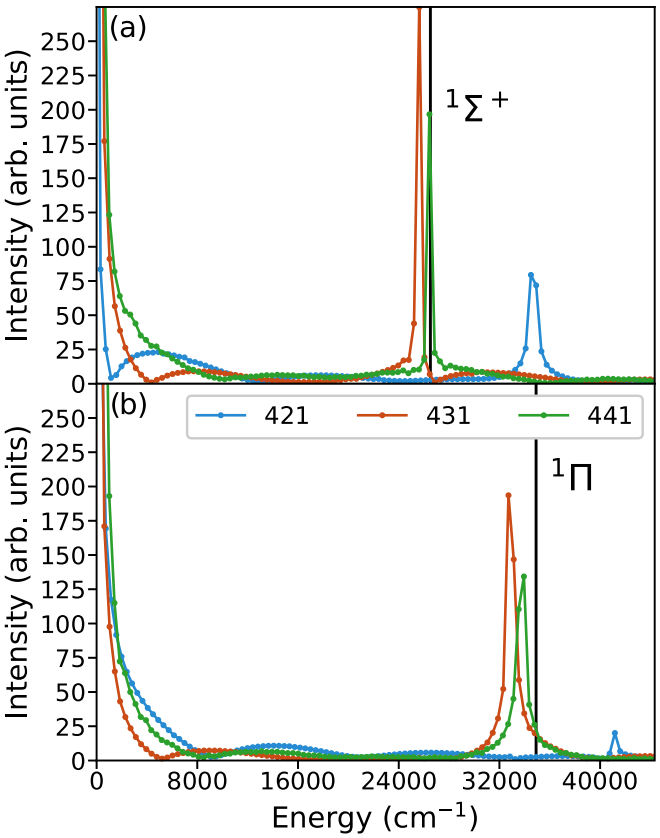

FIG. 5. Absorption spectra for LiH (cc-pVDZ basis set); experimental transition frequencies are marked with black lines [41,43]. (a) Excitation along the z polarization direction with different expansion lengths. (b) Excitation along the x polarization direction with different expansion lengths.

close agreement with the experiment, and can be chosen as a compromise between accuracy and computational demand. In the (421) expansion length, in which the electron-electron interaction is represented through mean-field interaction only with no correlation effects, the agreement with experiment is poor as expected.

Comparing to the H_2 spectra, it is very noticeable that for LiH, very little to no nuclear vibration is initiated, either through the laser pulse or the electronic motion.

In order to generate an electron-nuclear spectrum, a two-pulse excitation is carried out. First, LiH is irradiated using an infrared (IR) laser pulse to initiate nuclear motion, directly followed by the same laser pulse used prior to obtain the electronic spectrum. The resulting spectra are shown in Fig. 6, for the (441) expansion length and z or x polarization direction of the second pulse (parameters of the first pulse, $\omega = 0.010E_h$ (4556 nm), $I = 1.86\times10^{13}$ W/cm^2 (z-z) and $I = 2.19\times10^{13}$ W/cm^2 (z-x), $2\sigma = 60.8$ fs). The agreement of the calculated excitation energies with experimental transition energies is excellent. Two characteristics are very noticeable: Many small peaks at a similar energy spacing can be found in the spectra, which at least partially originate in nuclear excitations. Second, for Fig. 6(b), where the second laser pulse was polarized in the x direction, we also obtain excitation into the $^1\Sigma^+$ electronic state, which did not occur without nuclear

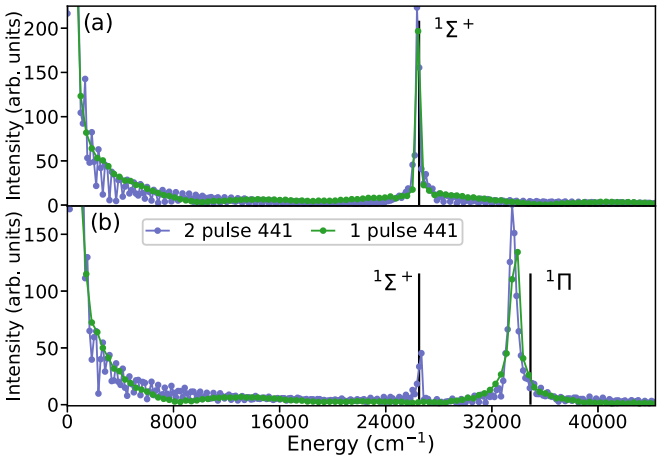

FIG. 6. Absorption spectra for LiH (cc-pVDZ basis set, (441) expansion length); experimental transition frequencies are marked with black lines [41,43]. The one-pulse spectrum is overlaid for comparison. (a) Excitation along the z polarization direction. (b) Excitation along the x polarization direction.

motion. Inducing nuclear motion therefore in turn induces a population transfer into the $^1\Sigma^+$ excited state.

An in-depth analysis of the two-pulse excitation spectrum is shown in Fig. 7, for the (441) expansion length and z polarization direction of both pulses. Many small peaks at a similar energy spacing can be found in the spectrum; however, for many of these it remains inconclusive if these represent real features in the electron-nuclear dynamics. The spacing between the small peaks is roughly 420–550 cm^{-1}, which is in the range of the experimental vibrational transition energies between the vibrational states in the $^1\Sigma^+$ state. But, as these features are very small, only peaks are discussed that exhibit substantial intensity and that are reproduced through different propagation times, and Fourier transforms of electronic and nuclear expectation values.

Different experimental vibrational and electronic transition energies [41,43] are marked on Fig. 7. In the higher-energy region, the $\nu_{0\text{-}0}$ transition energy coincides with the largest peak ($\sim$27 000 cm^{-1}), and several possible transitions lie around it, such as the $\nu_{1\text{-}1}$ and $\nu_{0\text{-}1}$ transitions. In the lower-energy region, the vibrational transition energies in the electronic ground state and $^1\Sigma^+$ excited state are marked as ν_0 and $\nu_0^{S_1}$ to ν_n and $\nu_n^{S_1}$, and so on for transitions from vibrational excited states. For LiH, no electronic transitions between the singlet excited states are observed in the spectrum ($^1\Pi \leftarrow {}^1\Sigma^+$) but only transitions from the electronic ground state.

C. Nuclear vibration of H_2 and LiH

The two above examples illustrate quite different electron-nuclear coupling effects. In the first example—H_2—the electronic motion leads to an uptake of nuclear motion, and to the appearance of many electronic and vibrational transitions in the spectra. In the second example—LiH—the induced nuclear motion influences the electronic excitations, and not only electronic and vibrational peaks are seen in the spectra but also transitions that were previously not observed, such as the $^1\Sigma^+$ excitation for the x polarization direction. The

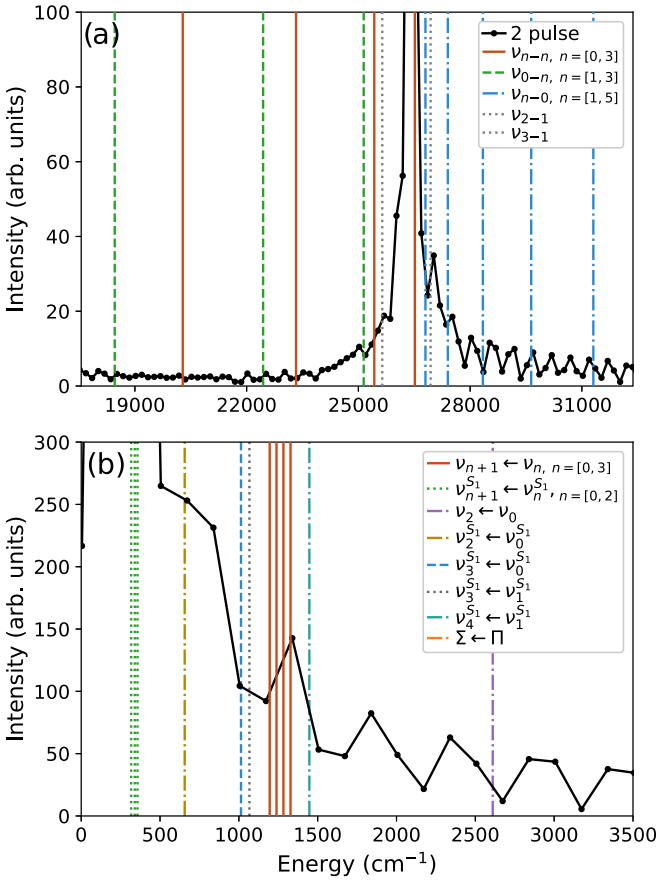

FIG. 7. Electronic and nuclear excitation peaks obtained from the two-pulse excitation of the (441) expansion length for LiH in the z polarization direction overlaid with experimental transition energies [41,43]. (a) The energy region around the first electronic excited state ($^1\Sigma^+$). (b) The energy region close to the electronic ground state.

nuclear vibration can also be visualized through the nuclear difference density.

The nuclear difference density in the grid basis, $\Delta\rho^n(R,t)$, which is the difference of the nuclear density at time t and initial time, can be obtained from

$$\Delta\rho^n(R,t) = \rho^n(R,t) - \rho^n(R,0), \tag{10}$$

with the nuclear density on the grid given as

$$\rho^n(R,t) = \sum_k^{n_{\mathrm{SPF}}} \sum_l^{n_{\mathrm{SPF}}} \sum_{j=1}^{J_{\max}} \phi_k^{n*}(R,t) A^*_{J,k}(t) A_{J,l}(t) \phi_l^n(R,t). \tag{11}$$

The sums here run over all SPFs k and l, and all their respective configurations J,k and J,l for a total number of configurations $J_{\max}$.

Such a nuclear density difference is shown in Fig. 8 for H_2. Already from the beginning of the propagation, just after the laser pulse has been switched off at about 3 fs, nuclear vibration sets in. Initially, the nuclei are moved further apart and move back to the equilibrium position; but around 32 fs, the nuclei start to move also further in, resulting in a vibration that leads to a shortening and stretching of the H_2 bond. The

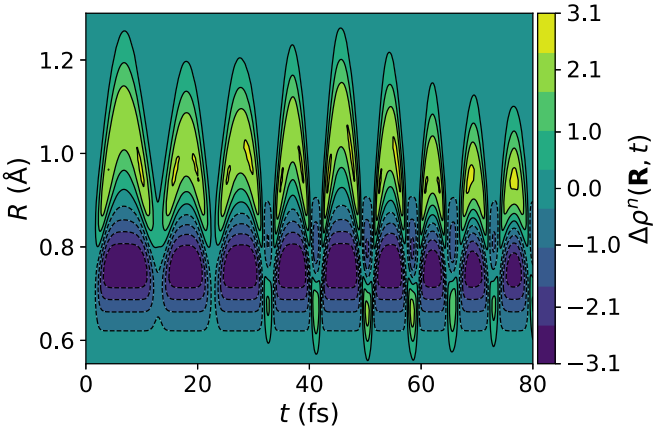

FIG. 8. Contour plot of the nuclear difference density $\Delta\rho_n(R,t)$ for H_2 during the excitation with a z-polarized laser pulse. Positive values indicate a probability increase, while negative contour values indicate a probability decrease.

vibrational period obtained with MCEND is 11.0 fs, which is close to the experimental vibrational period of H_2 (the fundamental vibrational excitation $\nu_0 = 4162.6\,\mathrm{cm}^{-1}$ has a vibrational period of ≈8 fs).

The difference density for LiH after laser-pulse excitation with an UV-visible wavelength is shown in Fig. 9(a) and results in very little nuclear motion, thus confirming the absence of vibrational peaks in the above spectra. For the two-pulse excitation, where an IR pulse is followed by an UV-visible pulse, the uptake of vibrational motion is clearly visible in the difference density, shown in Fig. 9(b). Here, the nuclear motion sets in around 20 fs and quickly builds up, with the nuclei moving in and out from the equilibrium position, resulting in a shortening and stretching of the bond and an oscillating nuclear contribution to the dipole moment.

D. Born-Oppenheimer potential and coherence properties

Monitoring the different energy contributions to the total energy allows a reconstruction of a time-varying "Born-Oppenheimer potential" which contains the overall potential energy contributions that can trigger nuclear motion. The Born-Oppenheimer (BO) potential is defined here as

$$V_{\mathrm{BO}}(t) = \langle T_e \rangle + \langle V_{ee} \rangle + \langle V_{en} \rangle + \langle V_{nn} \rangle \tag{12}$$

in analogy with the definition of potential energy surfaces. It should be noted at this point that the time dependence of the BO potential results from the implicit time dependence of its constituent terms; while the electronic kinetic energy, electron-electron interaction, etc., are defined as usual in a molecular Hamiltonian, their expectation values, of course, change over time due to the explicit time dependence of the wave function. As such, the time dependence of $V_{\mathrm{BO}}(t)$ results from the time dependence of the electron-nuclear wave packet.

The time-dependent BO potential is plotted against the nuclear distance expectation value R and time in Fig. 10. As the expectation values during the propagation are calculated at a time step of 0.01 fs, it is possible to generate an interpolated surface, although technically there is only

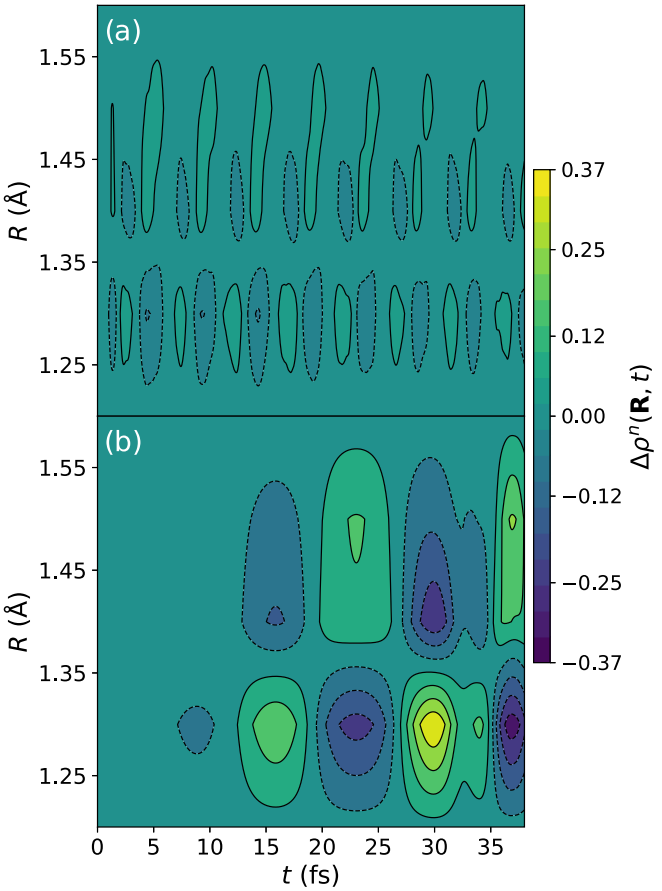

FIG. 9. Contour plot of the nuclear difference density $\Delta\rho_n(R,t)$ for LiH during the (a) UV-visible excitation using a pulse polarized along z and (b) an IR pulse followed by an UV-visible pulse to induce nuclear motion, both polarized along z.

one point for each t and R. The equilibrium bond distance before the laser pulse, which is the optimal bond distance for this basis set and expansion length as obtained through a propagation in imaginary time, is $R_0 = 0.763$ Å. Looking at the BO potential versus bond distance, the equilibrium distance no longer corresponds to a minimum in the potential. Instead, the minimum has been shifted to larger bond lengths

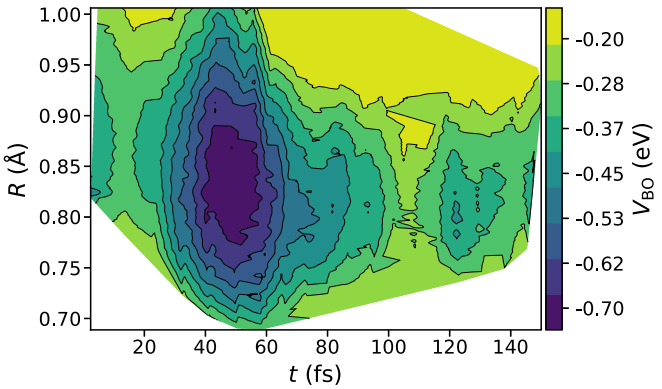

FIG. 10. Contour plot of the Born-Oppenheimer potential V_{BO} during the UV excitation of H_2 using a pulse polarized along z.

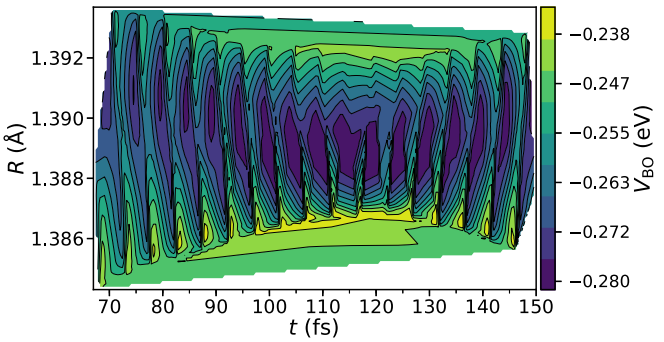

FIG. 11. Contour plot of the Born-Oppenheimer potential V_{BO} during the IR + visible excitation of LiH using a pulse polarized along z.

at around $R = 0.84$–0.90 Å. As the potential energy curves of the H_2 excited states are more repulsive with minimum bond lengths further out than the ground state, this overall behavior stems from the superposition of electronic ground and excited states that shifts the energy landscape. Also, for the first 40 fs, the BO potential does not reach any minima as deep as around 50 fs—although the bond lengths sampled during the propagation are the same. This reflects that not only the energetics but also the phase of the wave packet plays a significant role in the dynamics. Through the onset of nuclear motion, the electronic wave function loses coherence rapidly. The continuing modulation of the electronic wave function through the nuclear vibration, however, leads to recurrences of coherence in the electron-nuclear wave function and also, if the electronic ground state is significantly populated, to the reappearance of minima in the BO potential.

The time-dependent BO potential for LiH after the two-pulse excitation is shown in Fig. 11, and exhibits several minima at bond lengths further out from the equilibrium bond length (around $R = 1.392$ Å) and one minimum closer to the equilibrium bond length in the range $t = 110$–125 fs. Again, these minima occurring at certain times during the propagation are attributed to coherence and quantum transport effects: when the electronic part of the electron-nuclear wave packet mostly corresponds to the electronic ground state (around the equilibrium distance) versus electronic excited states (slightly elongated bond), and coherence is gained through the recurrence of resonances, then the BO potential exhibits dips that appear periodically, similar to quantum beats.

The coherence of a wave packet can be quantified through the density matrix ρ [44,45]. The density matrix contains the populations of the individual states on its diagonal, while the off-diagonal elements signify the mixing of the states. In a coherent wave packet, the phase of the wave packet has no destructive interference, and the trace of the density matrix squared—the purity P—is equal to 1. Decoherence of an initially coherent wave packet can be introduced through fluctuations of the environment, through which the purity is reduced, resembling a mixed state. Another measure of the mixture of a state is the von Neumann entropy S, given as

$$S = -\mathrm{tr}[\rho \ln \rho]. \tag{13}$$

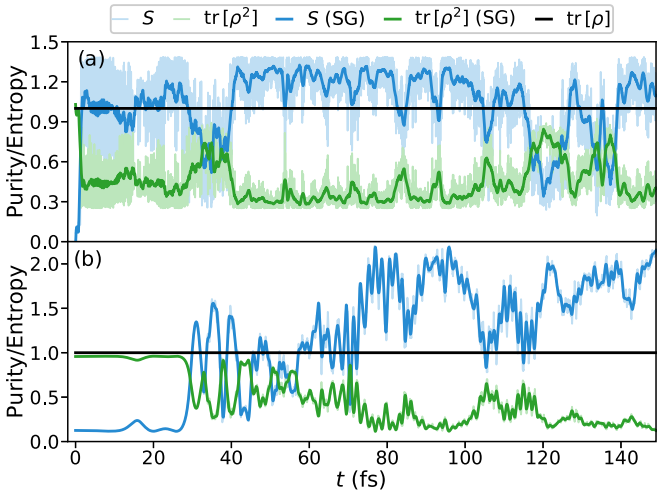

FIG. 12. Entropy S and purity $P = \mathrm{tr}[\rho^2]$ of the electron-nuclear wave packet as calculated from the density matrix. The norm $\mathrm{tr}[\rho]$ is shown as well to demonstrate the conservation of the norm. The raw data for S and P are overlaid with a filtered signal (Savitzky-Golay filter) for an enhancement of the dominant peaks (a) during the laser pulse excitation of H_2 and (b) during the two-pulse excitation of LiH.

If the nuclei in electron-nuclear dynamics are treated as classical particles, quantum coherence effects as well as effects from the spatial delocalization of the nuclear wave function are not present in the dynamics. Here, however, electrons and nuclei are treated on the same footing, and the electron-nuclear density matrix reflects the coherence and decoherence of the *molecular* wave packet. For H_2, initially an electronic wave packet is generated, but then the nuclear motion sets in quickly, leading to dephasing and a fast decoherence of the electronic wave packet in a few femtoseconds (Fig. 12). This is reflected in the quick rise of the entropy and lowering of the purity at the beginning of the propagation. However, throughout the propagation, the nuclear motion continuously modulates the electronic wave packet, while the electron dynamics modulate the nuclear motion—leading to recurrences of coherence as the purity increases around 38 and 120 fs, and the entropy decreases. These coherence gains are also visible in the BO potential as potential wells whenever the electronic wave packet mostly corresponds to the ground state.

For the two-pulse excitation in LiH, the underlying process is slightly different: in the first 60.8 fs, LiH is vibrationally excited with an IR laser pulse; coherence is maintained initially but then much reduced at around 25 fs. This is when the nuclear motion sets in fully (see above) and results from the electronic wave packet following the nuclei; though instantaneous, the following is not necessarily coherent during the rapid change of nuclear positions. At several instances throughout the propagation, entropy is reduced and purity gained. The change is not as dramatic as for H_2, and there are many more fluctuations obtained. The broad minimum in the BO potential around $t = 110$ fs coincides with one of these oscillations. So far, at this point we can conclude that several factors play a role in the occurrence and recurrence of the "dips" in the BO potential; one of them certainly is the coherence of the electron-nuclear wave packet, another the predominant population of one of the electronic states, and also the position of the nuclei, as we have shown throughout the two-pulse scheme that a small nuclear excitation can impact the electronic motion significantly.

IV. SUMMARY

Simulations of the fully coupled electron-nuclear dynamics of H_2 and LiH in strong laser fields demonstrated the high level of correlation between electronic and nuclear degrees of freedom. Excitation spectra of both diatomics contain signatures of the coupled motion, where for H_2, the electronic excitation directly initiated nuclear motion. In the case of LiH, nuclear motion was induced using a laser pulse, and then the electronic response was probed using a second pulse. Electronic transitions that are not observed under electronic excitation only for certain polarization directions could be obtained as a direct consequence of electron-nuclear coupling.

The time-dependent signatures of the potential that the nuclei experience due to electronic motion show recurring patterns that resemble quantum beating. The coherence properties of the electron-nuclear wave packets predominantly influence the occurrence of these minima in the potential.

Further investigations toward coupled electron-nuclear dynamics are needed to investigate the impact and magnitude of coherence effects, and their role in processes that exhibit, for example, quantum beating or other vibronic and excitonic states [46–49]. This is also important with respect to attosecond dynamics, as the experimental driving field for the generation of high-order harmonic radiation typically lies in the IR range [50], and the molecular response to the driving field can entail nuclear effects as well as the electronic motion [19].

ACKNOWLEDGMENTS

This work used the Extreme Science and Engineering Discovery Environment (XSEDE) [51], which is supported by NSF Grant No. ACI-1548562. The XSEDE resource Comet at the University of California, San Diego, was used for calculations through allocation TG-CHE170014. Acknowledgment is made to the donors of the American Chemical Society Petroleum Research Fund for support of this research via Grant No. 59762-ND6.

[1] P. M. Paul, E. S. Toma, P. Breger, G. Mullot, F. Auge, P. Balcou, H. G. Muller, and P. Agostini, Science **292**, 1689 (2001).

[2] M. Hentschel, R. Kienberger, C. Spielmann, G. A. Reider, N. Milosevic, T. Brabec, P. Corkum, U. Heinzmann, M. Drescher, and F. Krausz, Nature (London) **414**, 509 (2001).

[3] J. Itatani, J. Levesque, D. Zeidler, H. Niikura, H. Pépin, J. C. Kieffer, P. B. Corkum, and D. M. Villeneuve, Nature (London) **432**, 867 (2004).

[4] K. Zhao, Q. Zhang, M. Chini, Y. Wu, X. Wang, and Z. Chang, Opt. Lett. **37**, 3891 (2012).

[5] P. M. Kraus, B. Mignolet, D. Baykusheva, A. Rupenyan, L. Horný, E. F. Penka, G. Grassi, O. I. Tolstikhin, J. Schneider, F. Jensen, L. B. Madsen, A. D. Bandrauk, F. Remacle, and H. J. Wörner, Science **350**, 790 (2015).

[6] T. Stensitzki, Y. Yang, V. Kozich, A. A. Ahmed, F. Kössl, O. Kühn, and K. Heyne, Nat. Chem. **10**, 126 (2018).

[7] R. Weinkauf, P. Schanen, A. Metsala, E. W. Schlag, M. Bürgle, and H. Kessler, J. Phys. Chem. **100**, 18567 (1996).

[8] R. Weinkauf, E. W. Schlag, T. J. Martinez, and R. D. Levine, J. Phys. Chem. A **101**, 7702 (1997).

[9] F. Remacle, R. D. Levine, E. W. Schlag, and R. Weinkauf, J. Phys. Chem. **103**, 10149 (1999).

[10] L. S. Cederbaum and J. Zobeley, Chem. Phys. Lett. **307**, 205 (1999).

[11] A. I. Kuleff, S. Lünnemann, and L. S. Cederbaum, Chem. Phys. **414**, 100 (2013).

[12] A. I. Kuleff and L. S. Cederbaum, J. Phys. B: At. Mol. Opt. Phys. **47**, 124002 (2014).

[13] S. Chelkowski, T. Zuo, O. Atabek, and A. D. Bandrauk, Phys. Rev. A **52**, 2977 (1995).

[14] I. Znakovskaya, P. von den Hoff, S. Zherebtsov, A. Wirth, O. Herrwerth, M. J. J. Vrakking, R. de Vivie-Riedle, and M. F. Kling, Phys. Rev. Lett. **103**, 103002 (2009).

[15] W. Siu, F. Kelkensberg, G. Gademann, A. Rouzée, P. Johnsson, D. Dowek, M. Lucchini, F. Calegari, U. De Giovannini, A. Rubio, R. R. Lucchese, H. Kono, F. Lépine, and M. J. J. Vrakking, Phys. Rev. A **84**, 063412 (2011).

[16] I. Bocharova, R. Karimi, E. F. Penka, J. P. Brichta, P. Lassonde, X. Fu, J. C. Kieffer, A. D. Bandrauk, I. Litvinyuk, J. Sanderson, and F. Légaré, Phys. Rev. Lett. **107**, 063201 (2011).

[17] T. Kreibich, M. Lein, V. Engel, and E. K. U. Gross, Phys. Rev. Lett. **87**, 103901 (2001).

[18] Y. Cheng, M. Chini, X. Wang, A. González-Castrillo, A. Palacios, L. Argenti, F. Martín, and Z. Chang, Phys. Rev. A **94**, 023403 (2016).

[19] L. Cattaneo, J. Vos, R. Y. Bello, A. Palacios, S. Heuser, L. Pedrelli, M. Lucchini, C. Cirelli, F. Martín, and U. Keller, Nat. Phys. **14**, 733 (2018).

[20] M. Nest, Chem. Phys. Lett. **472**, 171 (2009).

[21] I. S. Ulusoy and M. Nest, J. Chem. Phys. **136**, 054112 (2012).

[22] I. S. Ulusoy and M. Nest, J. Phys. Chem. A **116**, 11107 (2012).

[23] M. H. Beck, A. Jäckle, G. Worth, and H.-D. Meyer, Phys. Rep. **324**, 1 (2000).

[24] T. Kato and H. Kono, Chem. Phys. Lett. **392**, 533 (2004).

[25] J. Caillat, J. Zanghellini, M. Kitzler, O. Koch, W. Kreuzer, and A. Scrinzi, Phys. Rev. A **71**, 012712 (2005).

[26] M. Nest, T. Klamroth, and P. Saalfrank, J. Chem. Phys. **122**, 124102 (2005).

[27] A. D. Bandrauk, S. Chelkowski, and H. S. Nguyen, Int. J. Quantum Chem. **100**, 834 (2004).

[28] K.-J. Yuan, H. Z. Lu, and A. D. Bandrauk, Phys. Rev. A **83**, 043418 (2011).

[29] A. Abedi, N. T. Maitra, and E. K. U. Gross, Phys. Rev. Lett. **105**, 123002 (2010).

[30] L. S. Cederbaum, J. Chem. Phys. **138**, 224110 (2013).

[31] E. Khosravi, A. Abedi, and N. T. Maitra, Phys. Rev. Lett. **115**, 263002 (2015).

[32] E. Deumens and Y. Öhrn, J. Phys. Chem. **92**, 3181 (1988).

[33] E. Deumens and Y. Öhrn, J. Phys. Chem. A **105**, 2660 (2001).

[34] E. Deumens and Y. Öhrn, Mol. Phys. **108**, 3195 (2010).

[35] B. F. E. Curchod, U. Rothlisberger, and I. Tavernelli, Chem. Phys. Chem. **14**, 1314 (2013).

[36] P. G. Lisinetskaya and R. Mitrić, Phys. Rev. A **83**, 033408 (2011).

[37] T. Nakatsukasa, K. Matsuyanagi, M. Matsuo, and K. Yabana, Rev. Mod. Phys. **88**, 045004 (2016).

[38] D. Skouteris, O. Gervasi, and A. Lagan, Chem. Phys. Lett. **500**, 144 (2010).

[39] D. J. Haxton, K. V. Lawler, and C. W. McCurdy, Phys. Rev. A **83**, 063416 (2011).

[40] P. Cassam-Chenaï, B. Suo, and W. Liu, Phys. Rev. A **92**, 012502 (2015).

[41] K. P. Huber and G. Herzberg, *Molecular Spectra and Molecular Structure—IV. Constants of Diatomic Molecules* (Van Nostrand Reinhold, New York, 1979).

[42] G. Herzberg and L. L. Howe, Can. J. Phys. **37**, 636 (1959).

[43] W. C. Stwalley and W. T. Zemke, J. Phys. Chem. Ref. Data **22**, 87 (1993).

[44] M. Vacher, M. J. Bearpark, M. A. Robb, and J. P. Malhado, Phys. Rev. Lett. **118**, 083001 (2017).

[45] C. Arnold, O. Vendrell, and R. Santra, Phys. Rev. A **95**, 033425 (2017).

[46] V. Tiwari, W. K. Peters, and D. M. Jonas, Proc. Natl. Acad. Sci. USA **110**, 1203 (2013).

[47] D. P. Hoffman and R. A. Mathies, Acc. Chem. Res. **49**, 616 (2016).

[48] F. Holzmeier, R. Y. Bello, M. Hervé, A. Achner, T. M. Baumann, M. Meyer, P. Finetti, M. Di Fraia, D. Gauthier, E. Roussel, O. Plekan, R. Richter, K. C. Prince, C. Callegari, H. Bachau, A. Palacios, F. Martín, and D. Dowek, Phys. Rev. Lett. **121**, 103002 (2018).

[49] D. Jelovina, J. Feist, F. Martín, and A. Palacios, New J. Phys. **20**, 123004 (2018).

[50] D. Baykusheva, P. M. Kraus, S. B. Zhang, N. Rohringer, and H. J. Wörner, Faraday Discuss. **171**, 113 (2014).

[51] J. Towns, T. Cockerill, M. Dahan, I. Foster, K. Gaither, A. Grimshaw, V. Hazlewood, S. Lathrop, D. Lifka, G. D. Peterson, R. Roskies, J. R. Scott, and N. Wilkins-Diehr, Comput. Sci. Eng. **16**, 62 (2014).